ChemPubSoc Europe

DOI: 10.1002/slct.201600090

Chemistry SELECT Full Papers

Catalysis

# High Energy Ball-Milling Synthesis of Nanostructured Ag-Doped and $BiVO_4$-Based Photocatalysts

Victor Ishrayelu Merupo,[a, b] Subramaniam Velumani,*[a] Goldie Oza,[a] Mohamed Tabellout,[b] Monserrat Bizarro,[c] Sandrine Coste,[b] and Abdel Hadi Kassiba*[b]

Nanostructured composites based on plasmonic Ag metal nanoclusters with monoclinc-$BiVO_4$ nanoparticles were prepared by high energy ball milling technique. The agglomerated morphology with a spherical shape of 50–100 nm sized $BiVO_4$ particles associated with homogeneous distribution of 5–10 nm Ag clusters significantly enhanced the photocatalytic activity for the degradation of acid blue dyes. The Ag doping concentration with $BiVO_4$ was optimized at 3 at. % leading to almost 10 folds faster photocatalytic degradation rate as compared to pristine form. Thus, Ag doped $BiVO_4$ nanocomposites show efficient visible light driven photocatalytic activity due to charge distribution at the semiconducting-metal interfaces from band bending and the involvement of a radiation field enhanced by plasmon resonance effects at the surfaces of Ag-clusters.

## Introduction

Visible light driven photocatalyst plays a key role in promoting chemical reactions under the abundant and renewable energy source as sunlight. In this context, heterogeneous photocatalysis can provide reliable solutions for several environmental challenges by harvesting the solar radiation to ensure efficient chemical reactions. Followed by the first report on auto-oxidation (1956), Honda and Fujishima demonstrated electrochemical photolysis using semiconductor $TiO_2$.[1] Since then, semiconductor photocatalysts has received a great attention due to its various potential applications with two major approaches:

- Decomposition of organic groups in either aqueous solutions or in defined atmospheres. This is so-called environmental remediation process which is extensively investigated during the last two decades as a function of several classes of photocatalysts and nature of pollutants.
- Water splitting for the production of hydrogen gas, which is able to replace fossil fuels with an aim to reduce $CO_2$ emission.

In general, $TiO_2$ is the most investigated semiconducting photocatalyst.[2] However, due to its large band gap (~3.2 eV), photocatalysis occurs under UV radiation (<388 nm) which is just 4–6% of the solar radiation. This wide band gap inhibits the harvesting of $TiO_2$ under visible light radiations which is 43% of the solar spectrum. In this context, $BiVO_4$ is a challenging material as a visible light –driven photocatalyst.[3–6] However, $BiVO_4$ exists in three main crystalline polymorphs viz, monoclinic, tetragonal scheelite and tetragonal zircon.[7] The monoclinic phase $BiVO_4$ is expected to be more efficient in photo-redox applications with regard to its narrow band gap (~2.4 eV). Moreover, band edge positions which occurs from distorted local environments of $V^{5+}$, $Bi^{3+}$ ions and availability of Bi $6s^2$ lone pairs contributes to the electronic structure[8] which enhances the photo-excitation process. The photocatalytic performance depends upon the quantum efficiency of the photoactive system. However, for semiconducting systems, a major drawback lies in the large amount of photogenerated charge carriers being inhibited by a fast recombination process with quite low characteristic lifetimes (~$10^{-9}$ sec). On the other hand, though semiconductors with narrow electronic band gaps harvest broad radiation spectral range, they are highly vulnerable to photo-corrosion. To address these issues, intense investigations were carried out through chemical modifications of photocatalysts to overcome the fast photo induced charge carrier recombination as well as inhibition of photo-corrosion phenomena notably by deposition of a suitable co-catalyst on the surface of the photoactive semiconductor media.[9,10] It is also highly relevant to consider photocatalysts exploiting plasmonic effects induced by the incorporation or decoration of semiconducting surfaces with metallic nanoparticles (NMNPs) such as Au, Ag, Pt etc. By this means, an enhancement of the density of photogenerated electron-hole pairs is expected along with longer recombination times.[11] Moreover, incorporation of plasmonic supports such as Au, Ag and Pt clusters would extend the absorption in visible light due to Localized Surface Plasmon Resonance (LSPR) effect able to

[a] *Dr. V. I. Merupo, Prof. S. Velumani, Dr. G. Oza*
Department of Electrical Engineering (SEES),
CINVESTAV-IPN,
Av IPN #2508, Col Zacatenco, D.F., C.P. 07360, Mexico
E-mail: velu@cinvestav.mx

[b] *Dr. V. I. Merupo, Dr. M. Tabellout, Dr. S. Coste, Prof. A. H. Kassiba*
Institute of Molecules & Materials of Le Mans (IMMM) UMR CNRS, Université du Maine,
72085 Le Mans, France
E-mail: kassiba@univ-lemans.fr

[c] *Dr. M. Bizarro*
Institute of Investigaciones en Materiales,
Universidad Nacional Autónoma de México,
A.P. 70–360, Coyoacán C.P. 04510, D.F., Mexico

Supporting information for this article is available on the WWW under http://dx.doi.org/10.1002/slct.201600090

improve photocatalytic performance.[12,13] So far, Ag/$BiVO_4$ composites were synthesized by several chemical routes such as hydrothermal techniques,[14] solvo-thermal technique,[15] photo deposited method,[16] and wet impregnation method.[17] It was reported that 10–20 nm Ag particles located on $BiVO_4$ thin films deposited by modified metal organic decomposition technique has shown nearly two times higher degradation of phenol compared to pristine thin films.[18]

In this contribution, we report for the first time a physical route technique i.e. high energy ball milling (HEM) for the synthesis of Ag-$BiVO_4$ nanocomposites along with its physico-chemical features and photochemical reactivity.[19] Exhaustive analyses were performed by HR-TEM and FE-SEM to probe the structure, morphology and organization of the nanocomposites. From the dielectric measurements, electrical conductivity and polarization effects were determined and correlate with the density of metal-semiconductor interfaces involved at nano-scale between metallic clusters and $BiVO_4$ nanoparticles. The optical features were analyzed including the evaluation of the optical band gap as a function of Ag doping ratios. The photocatalytic activity of Ag/$BiVO_4$ nanocomposites was evaluated by the ability to degrade acid blue 113 (AB 113) dyes. The kinetics of the reactions were determined and compared as a function of Ag doping ratios compared to pure host $BiVO_4$ structure. A simple model dealing with the electronic features at the interfaces of metal-semiconductor was proposed to address the correlation between the Ag content and the photocatalytic efficiency. The approach takes into account the Schottky barriers (Ag-$BiVO_4$) as well as the role of surface plasmon originating from Ag clusters.

In the results and discussion section, the prepared samples were referred as A, B, C and D for pristine $BiVO_4$, 1 at. %, 3 at.% and 5 at.% of silver loading in Ag/$BiVO_4$ nanocomposites respectively.

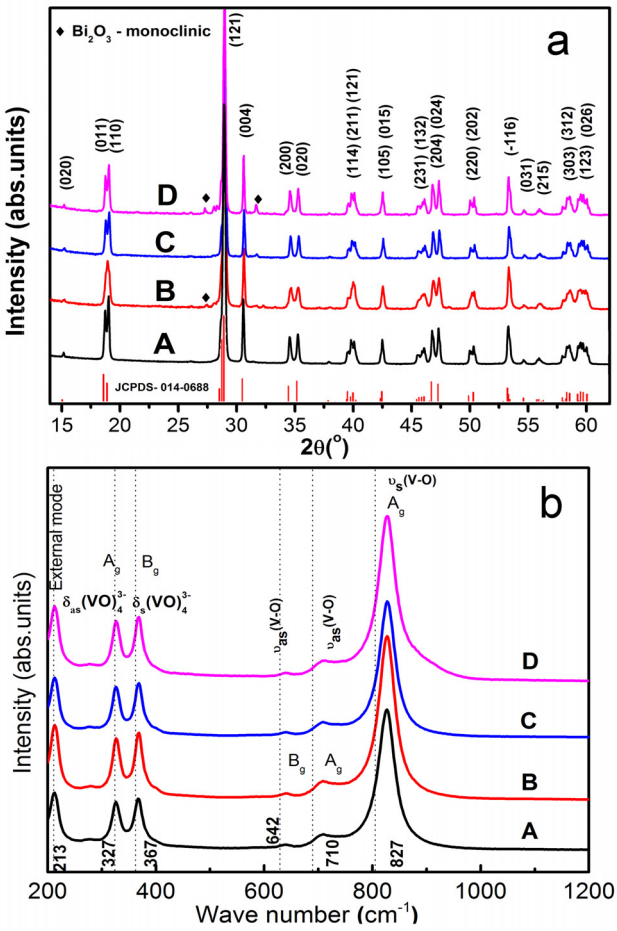


**Figure 1. a:** X-ray powder diffraction patterns of Ag/$BiVO_4$ nanoparticle prepared by ball milling technique. The bottom plot in Figure 1a represent the reference pattern for monoclinic $BiVO_4$ (JCPDS - 14–0688). **b:** Raman spectra of Ag/$BiVO_4$ nanoparticles.

## Results and Discussion

### Structural features:

The crystal structure of the Ag/$BiVO_4$ nanocomposites synthesized by ball milling technique was studied by XRD and micro-Raman techniques. All the powder samples have shown monoclinic scheelite phase with characteristic peaks in agreement with JCPDS data card (No: 14–0688) depicted in Figure 1a. However, there is no distortion in monoclinic scheelite phase as well as no obvious diffraction peaks of the silver based compounds. Thus, Ag doping did not affect the crystal structure of $BiVO_4$[20,21] and seems to indicate that silver nanoclusters are homogeneously distributed in the host semiconductor (Figure 3). Crystalline domain sizes of $BiVO_4$ and Ag/$BiVO_4$ were estimated from Scherrer's formula and reported in Table 1. The calculations consider the XRD line broadening FWHM values subtracted from the standard FWHM of the used reference $LaB_6$ fixed at $\Delta(2\theta) = 0.046^\circ$. The average size of the crystalline domains for Ag/$BiVO_4$ nanocomposites were situated in the range of 35–50 nm. The Raman spectra of monoclinic $BiVO_4$ has five distinguishable vibrational bands located at 210, 327, 367, 710 and 827 $cm^{-1}$ as shown in Figure 1b. The vibrational mode at 210 $cm^{-1}$ is the external mode of monoclinic $BiVO_4$. Remaining modes are related to $VO_4$ tetrahedron bond vibrations. Two sets of stretching modes for V–O bonds consist of symmetric $A_g$ at 827 and asymmetric $A_g$ 710 $cm^{-1}$. Similarly, the symmetric ($A_g$) and anti-symmetric ($B_g$) bending modes occur at 367 and 327 $cm^{-1}$ respectively. The Raman spectra of Ag/$BiVO_4$ traduce the features of monoclinic phase for the host structure without substantial changes with Ag loading in contrast to other reports on some metal doped semiconductor materials.[22,23]

**Table 1.** Calculated crystal domain sizes from Scherrer's formula.

| | Samples | Crystallite size(nm) |
|---|---|---|
| A | $BiVO_4$ | 45.78 ± 0.78 |
| B | 1at.% Ag/$BiVO_4$ | 37.07 ± 1.86 |
| C | 3at.% Ag/$BiVO_4$ | 43.93 ± 1.31 |
| D | 5at.% Ag/$BiVO_4$ | 48.29 ± 1.44 |

**Morphological studies:**

FE-SEM images of Ag/$BiVO_4$ nanocomposites (Figure 2) show heavily agglomerated spherical particles with sizes around

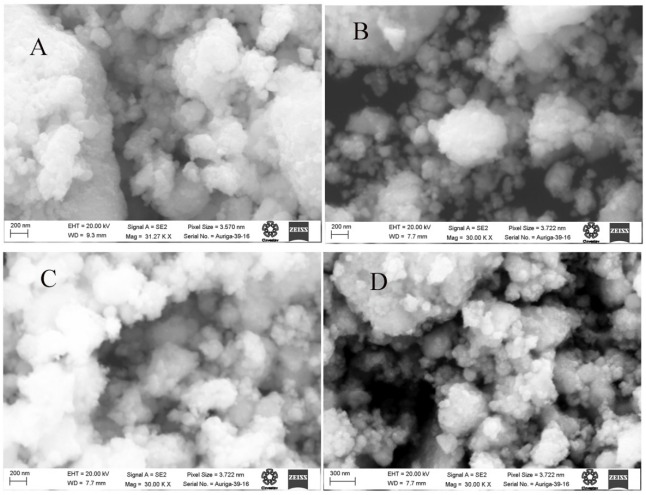


**Figure 2.** Morphologies of Ag/$BiVO_4$ nanocomposites from FE-SEM.

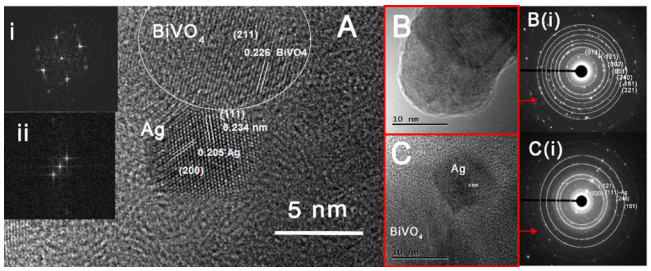


**Figure 3.** High resolution HR-TEM images of 5 at.% Ag/$BiVO_4$ nanocomposites. (A) An enlarged HR-TEM image of $BiVO_4$ grain and Ag cluster. Insets (i) and (ii) show fast FFT patterns of Ag and $BiVO_4$ parts from A. B and C of pure $BiVO_4$ and Ag/$BiVO_4$ composites with corresponding SAED patterns in **3B(i)** and **3C(i)** respectively.

**UV-Vis spectroscopy analysis**

The electronic structure of semiconductors can be revealed by the interaction of light under defined wavelengths. The crystalline structure, morphology and doping by suitable elements modulate the electronic and optical features which can be fine-tuned to harvest defined spectral range of light. Beyond such

**Table 2.** Chemical composition of Ag/$BiVO_4$ nanocomposites from EDAX

| | Ag (at. %) Experimental | Ag (at.%) (EDS) | Bismuth (at. %) | Vanadium (at. %) | Oxygen (at. %) |
|---|---|---|---|---|---|
| A | 0 | 0 | 19.05 | 20.20 | 60.75 |
| B | 1 | 0.40 ± 0.05 | 20.42 | 20.48 | 58.68 |
| C | 3 | 0.78 ± 0.08 | 19.49 | 20.17 | 59.55 |
| D | 5 | 1.30 ± 0.05 | 19.30 | 18.99 | 60.41 |

50–80 nm. Agglomerations may occur from the high surface energy and inter-particle forces induced by strong collisions between reactants and hard phase balls in the synthesis process. Quantitative chemical analysis of Ag/$BiVO_4$ nanoparticle by EDAX is summarized in Table 2. Doping Ag content has been identified by EDAX less to the experimental value that might be due to the capability of EDAX to probe the chemical composition on wide area of the sample and also the possible inhomogeneous distribution of Ag clusters in the nanocomposites. High-resolution transmission electron microscopy (HR-TEM) images reveal well crystallized domains through resolved monoclinic lattice fringes as illustrated in Figure 3 for the sample doped by 5 at.% Ag /$BiVO_4$ . The observed lattice fringes with reticular spacing of 0.226 nm are consistent with (211) plane of monoclinic $BiVO_4$. In addition, separate lattice fringes with a spacing of about 0.205 nm and 0.224 nm are clearly observed in Figure 3A, which is in agreement with (200) and (111) lattice planes of the crystalline silver lattice superimposed to $BiVO_4$ structure. Selected areas were probed by electron diffraction (SAED) performed on pure $BiVO_4$ (Figure 3B) and on 5 at.% Ag/$BiVO_4$ (Figure 3C). The obtained patterns are shown in 3B(i) and 3C(i) for pure and 5at.% Ag/$BiVO_4$ samples respectively.[10]

approaches, the exploitation of plasmonic effects is worthy of interest to act efficiently on the optical features of the photoactive materials[24] as we propose to demonstrate on Ag/ $BiVO_4$ nanocomposites. Thus, diffuse reflectance UV-Vis spectra of Ag/ $BiVO_4$ plasmonic photocatalysts were recorded for different silver loading ratios as summarized in Figure 4. In plasmonic photocatalysts, the metal clusters with oscillating electrons possess dipolar nature, which in turn enhances local electric fields and related energy radiates in neighboring semiconducting particles. This effect enlarges the absorption bands in the visible range as shown in the comparative absorption spectra depicted in Figure 4 for Ag/$BiVO_4$ nanocomposites. Gradual increment in spectral absorption at 520 nm with Ag loading ratios correlates with LSPR effect originating from Ag nanoclusters. Furthermore, it is also demonstrated that as compared to pure $BiVO_4$, the absorption edge of Ag/$BiVO_4$ nanocomposites undergoes red shift which correlates with increased Ag loading ratios and silver cluster sizes [25]. At the interfaces of semiconductor- metal, plasmonic effect can produce an optical field enhancing the intensity of optical absorption bands. The relationship of absorbance and incident photon energy hν can be described in Eq. (1) for direct valence band to conduction band transitions:

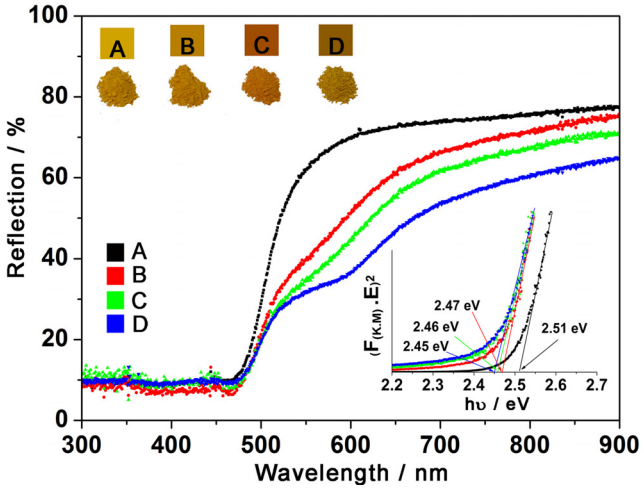


**Figure 4.** Diffuse reflective spectra with inset Tauc plot of $Ag/BiVO_4$ along with colour of nanocomposites after annealing at 450°C.

$$\alpha h = A[h\nu - E_g]^{1/2} \quad (1)$$

From the Tauc plot, an evaluation was made for the electronic band gap. The obtained values vary slightly between 2.51 eV for pristine to 2.45 eV for Ag concentration. The slight shift in the band gaps with increased doping ratios indicates a weak substitution of Ag inside the host $BiVO_4$ matrix. This result is consistent with the formation of Ag clusters segregated from $BiVO_4$ particles.

### Dielectric investigations

The dielectric behavior of the pure sample was compared to one of the representative Ag doped samples; i.e. 3 at. % Ag-$BiVO_4$. The relative complex permittivity functions $\varepsilon^*(\omega, T) = \varepsilon'(\omega, T) - i\varepsilon''(\omega, T)$ were obtained by applied alternative voltage with frequency $(\omega/2\pi)$ at different temperatures from 273 K to 473 K with an interval of 20 K. The phenomenological model used to account for the complex permittivity $\varepsilon^*(\omega, T)$ consists in the well-known Havriliak–Negami (HN) relaxation model.[26]

$$\varepsilon^*(\omega, T) = \frac{\sigma_{dc}}{i\omega\varepsilon_0} + \varepsilon_\infty + \frac{\Delta\varepsilon}{((1+i\omega\tau)^\alpha)^\beta} \quad (2)$$

In this expression, dielectric strength $\Delta\varepsilon$ represents the difference between the quasi-static dielectric permittivity $\varepsilon_s$ and the high frequency one $'\varepsilon_\infty'$. The characteristic time coefficient $\tau$ is associated to the dielectric relaxation phenomena which also closely related to conductivity processes as discussed below. The phenomenological parameters $\alpha$ and $\beta$, in the range $0 < (\alpha, \beta) < 1$, traduce the distribution of relaxation times due to some inhomogeneous processes which may be induced by nanocrystallite sizes or surface effects on $BiVO_4$ nanoparticles. In the simple case of Arrhenius model, the dielectric relaxation is characterized by a unique relaxation time $\tau_0$ leading to $\alpha = 1$ and $\beta = 1$. For a general case, we may only give the asymptotic behavior of $\varepsilon''(\omega)$ in the low and high frequency range with respect to the characteristic relaxation times. The tendencies are expressed in terms of $\alpha$ and $\beta$ such as $\varepsilon'' \propto \omega^\alpha$ when $\omega\tau \ll 1$ and $\varepsilon'' \propto \omega^{\alpha\beta}$ for $\omega\tau \gg 1$. From the plot of dielectric functions, the characteristic time $\tau$ correlates with the frequency where the maximum of dielectric loss peak is located. The coefficients $\alpha$ and $\beta$ are evaluated by fitting experimental curves according to Eq. (2). In HN simulation, the same set of fitting parameters were used for both real and imaginary parts of dielectric function as well as for the frequency dependent conductivity. Figure 5(a, b) summarizes the experimental results for real and imaginary parts of the relative complex dielectric permittivity related to the pure sample and to the 3 at. % Ag/$BiVO_4$ nanocomposite. The frequency dependence of the dielectric function reflects dynamic processes with thermally dependent relaxation phenomena. The dielectric behavior at low frequencies manifested through the divergence of $\varepsilon'(\omega)$ is related to electrode polarization induced by ionic conductivity being thermally activated with increasing temperature. The low frequency (LF) which shows a divergent contribution is no longer relevant to the intrinsic dielectric behavior of the materials. Thus, the fitting of dielectric data is well accounted by HN model depicted as continuous lines in Figure 5, 6(1 a, 2 a). The calculated asymptotic behavior of $\varepsilon'(\omega)$ in the quasi-static regime is assigned to the dielectric constant which is indicative of large interfacial polarizations. Indeed, the quasi-static values of $\varepsilon'(\omega)$ are approximately around 80 and 140 for pure and 3at. % Ag loading concentration respectively. Compared to pristine $BiVO_4$, $Ag/BiVO_4$ composite structures possess higher dielectric constant values due to interfacial polarization induced by metal (Ag)-semiconductor (SC) interfaces with Ag clusters.

The relaxation times characterize the dynamics of dipolar relaxation process or mobility of charge carriers induced in the samples by alternative voltages. A distribution of relaxation times (DRT) is more relevant to define the shape of the dielectric functions accounted by HN model (Figure 6b). The dielectric behavior of pure $BiVO_4$ particles is marked by a unique relaxation regime in the whole temperature range. For Ag loaded $BiVO_4$, two relaxation regimes are involved in the low temperature range 273–373 K and for higher temperature range 373–473 K. Such behavior is understood from the incorporation of Ag clusters in the composite with modified interfacial polarizations and mobility of charge carriers as well. This last effect is traduced by the slight increase in the effective conductivity of the doped sample. In addition to the relaxation peculiarities, the thermal evolution of the dc conductivities is also modified by silver loading where the activation energies of charge carriers depend on the temperature range. Indeed, semi-log plot of $\sigma^i_{dc}$ versus the inverse of temperature 1000/ T (K) is reported in Figure 7 and exhibits quite complex behavior depending on the temperature range and the composition of the sample. The conductivity is thermally activated as $\sigma^i_{dc}(T) = \sigma^{i0}_{dc} e^{-\frac{E_a}{kT}}$ with the activation energy estimated by fitting the experimental data. Thus, 0.36 eV was obtained for pure sample in the temperature range (373—473 K) while the doped sample (3 at %), gives

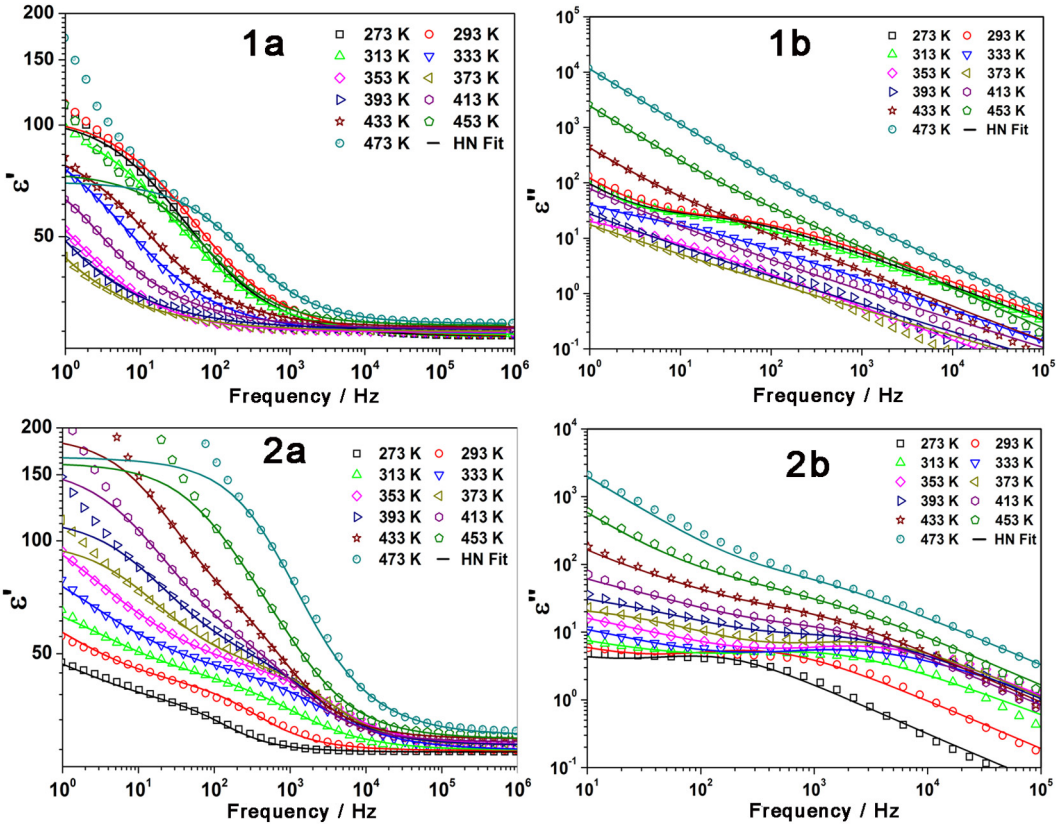


**Figure 5.** Temperature and frequency dependencies of (a) real dielectric permittivity, (b) imaginary dielectric permittivity for (1) pristine (2) 3 at. % Ag/ $BiVO_4$ sample. The continuous lines are fits obtained by Havriliak–Negami model.

0.06 eV and 0.3 eV as activation energies in the temperature ranges (273–373 K) and (373–473 K) respectively. The low activation energy and a higher conductivity in the doped sample indicate low barrier heights involved in the conduction channels depending also on the microstructure and composition of the samples. Indeed, the nature of the interfaces is quite different from pure and Ag doped samples. SC-SC interfaces in pure sample may show a high density of dangling bonds acting as traps for charge transfer between adjacent SC particles. For doped sample with SC—Ag interfaces, the density of dangling bonds is expected to be less with regard to metallic Ag clusters which facilitate the charge distribution between the surrounding particles. The slope change in the logarithmic representation of $\sigma_{dc}^{j}(T)$versus 1000/ T (K) was observed in pure sample, irrespective of the synthesis method (sol-gel, ball milling). This singular behavior is no longer characteristic of pure SC features where the conductivity is thermally activated with an increase in the charge carrier density with the temperature. The behavior of the conductivity below 353 K suggests the existence of a population of free electrons which may occur due to the departure from stoichiometry. As a consequence, the occurrence of oxygen vacancies is accompanied by mixed oxidation degrees of vanadium ions already demonstrated in pure $BiVO_4$ from EPR investigations.[27] The substantial concentration of $V^{4+}$ observed instead of $V^{5+}$ is indicative of oxygen vacancies. Oppositely Ag doped composites show activated conductivity with only changes on the activation energy as function of the considered temperature ranges

To sum up, the thermally activated conductivity at 473 K for pure and 3 at.% doped Ag/$BiVO_4$ nanocomposites are 7 x $10^{-9}$ and 1.5 x $10^{-8}$ S/cm respectively. In the pure sample, two main thermal evolution regimes were demonstrated with cross-over at critical temperature about 353 K. The activation energies depend on the considered temperature ranges, on the composition, microstructure and crystalline order of the samples which modulate the height of barriers acting on the conduction channels. The charge carrier mobility is expected to be optimal in 3 at. % Ag loaded $BiVO_4$. This optimized carrier mobility in combination with plasmonic effect involved on the surfaces of Ag nanoclusters can contribute to efficient plasmonic photocatalysis as will be discussed below.

## Photocatalysis investigations

The photocatalytic activity of the Ag/$BiVO_4$ samples were investigated through the degradation of AB 113 dyes in aqueous solutions. AB 113 is double azo based dyes and the optical behavior is characterized by a main absorption band located at 566 nm and assigned to n– π* transition of –N = N– group. The second less intense band centered at 280 nm is attributed to the ligand center (π–π*) transition related to the naphthalene ring attached to the –N = N– bonds as depicted in Fig-

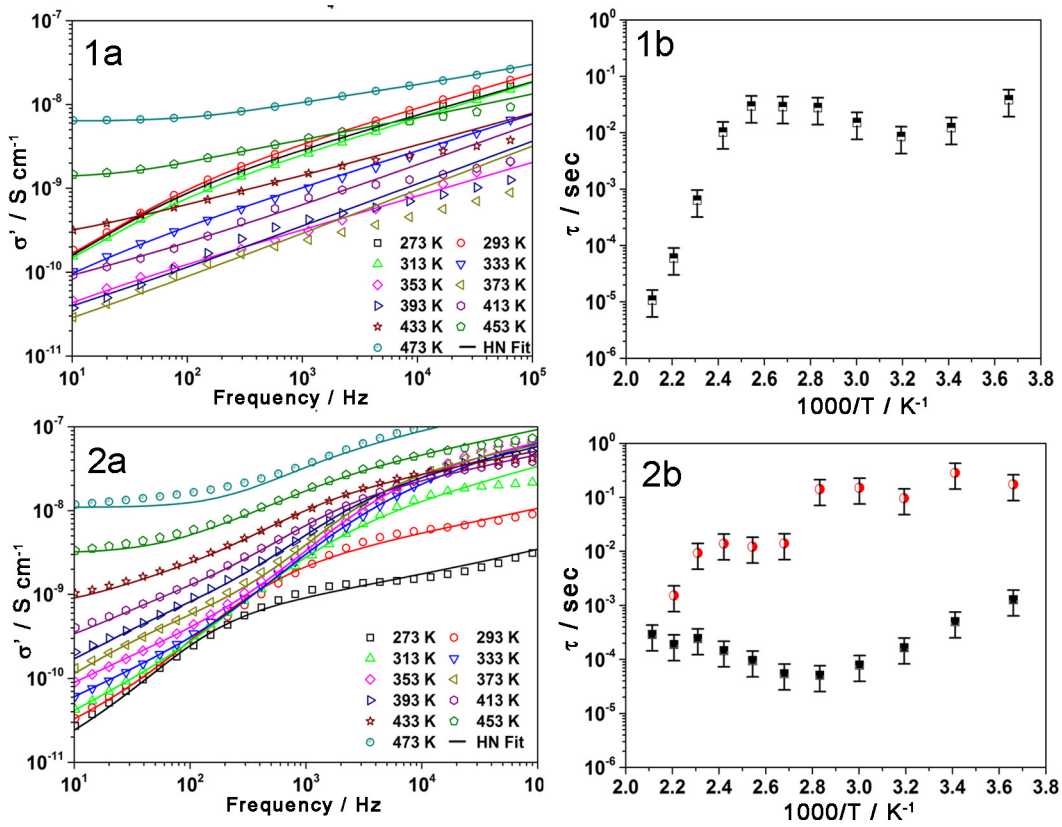


**Figure 6.** Temperature and frequency dependencies of (a) Frequency dependent (ac) of real part of conductivity $\sigma_{dc}$ and (b) variation of the relaxation times for different temperatures for (1) pristine (2) 3at.% Ag/ $BiVO_4$ sample. The continuous lines are fits obtained by Havriliak–Negami model.

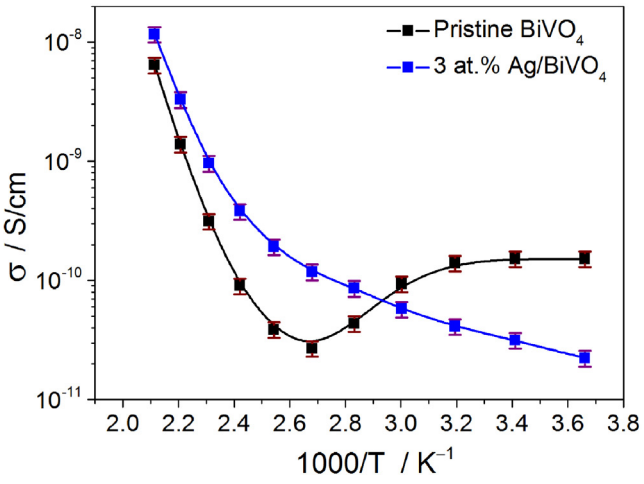


**Figure 7.** DC-conductivity versus inverse temperature plots for pristine and 3 at. % Ag/ $BiVO_4$ samples.

ure S1 in supporting information along with its chemical structure in inset. The reported work has identified AB 113 as one of potential carcinogenic agent[28] widely used in wool coloring to obtain deep shade of navy blue color in industrial textile. Due to the presence of large degree of organics and stability of the dyes, conventional methods (chemical, filtration) are inefficient for its removal. Thus, the visible light driven photoinduced process for the degradation of AB 113 is an ambitious task.

### Kinetics of AB 113 photodegradation

Photocatalytic investigations based on Ag/ $BiVO_4$ were carried out by adding powder samples with different Ag doping ratios to solutions with a fixed molar concentration of AB 113 dyes ($10^{-5}$ M). A given solution was first stirred for 20 min under dark to reach absorption/ desorption equilibrium. At this stage, AB 113 charged solutions containing 0, 1, 3 and 5at. % Ag loaded $BiVO_4$ powders showed a degradation rate of 22%, 33% 38% and 24% respectively. Under Xe-lamp with an irradiation intensity of 1.5 W/$cm^2$ at the level of the sample, the photoactive solution charged with 1at.% and 3at.% Ag doped $BiVO_4$ powders show the most efficient photocatalytic activity. The effect is traduced by the rapid decrement in the absorption band intensity at 566 nm testifying efficient degradation of the azo groups. Comparative photocatalytic activities between the different Ag loaded samples (Figure 8a) indicate that the 3at. % Ag doped $BiVO_4$ exhibits 2.5 times higher efficiency as compared to the pure sample. For a higher Ag loading (5 at. %), the degradation rate didn't show any improvement as compared to pure $BiVO_4$. Several reasons may be invoked such as the non-homogeneous distribution of Ag nanoclusters in the host media or the increase in the sample disorder with limited electrical

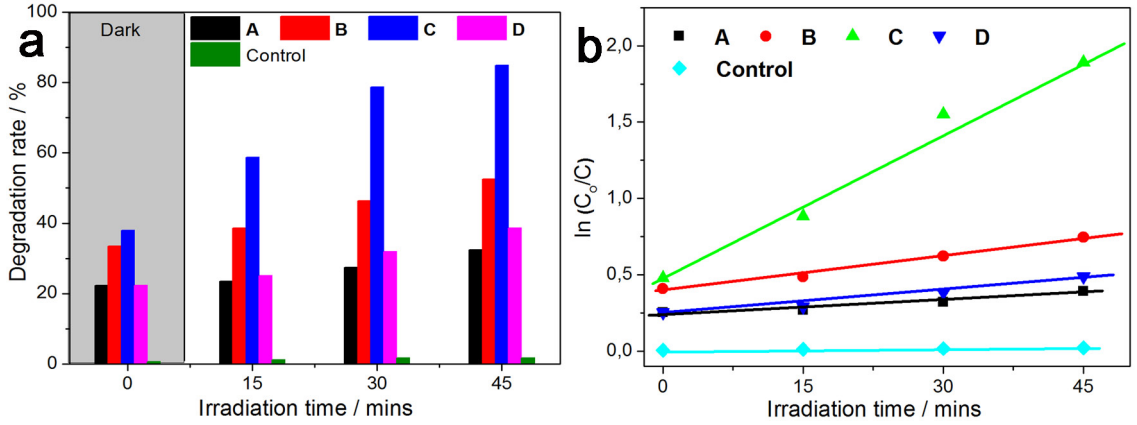


**Figure 8. A:** Kinetic analysis of photocatalytic degradation of AB 113 probed by the absorbance at room temperature, **B:** pseudo-first-order kinetics of degradation of AB 113 diazo in solution through the time dependence of the dyes concentration.

conductivity as evaluated in the above section versus the doping ratios. A similar trend has been reported for hydrothermally synthesized Ag doped $BiVO_4$ particles.[20]

The degradation kinetic analysis of AB113 dyes by Ag/$BiVO_4$ (Figure 8b) was made according to the following relation:

$$[C]_t = [C]_0\ e^{-tk} \quad (3)$$

Where $[C]_0$ represents the initial concentration, $[C]_t$ is the measured concentration at an irradiation time t and k is the degradation rate constant or pseudo-first-order rate constant. The carried out experiments and their analysis give the rate of degradation constant values as a function of the Ag loading (Table 3).

**Table 3.** Pseudo first-order degradation rate constant of AB113 dye in the presence of Ag/$BiVO_4$ with different loading content of silver.

| | Doping rates of Ag/$BiVO_4$ (at.%) | Degradation rate constant, k ($min^{-1}$) ± error | Remaining percent of AB113 after radiation for 45 min (%) |
|---|---|---|---|
| A | 0 | 0.004 ± 2.6e–4 | 67.6 |
| B | 1 | 0.008 ± 1.7e–4 | 47.5 |
| C | 3 | 0.032 ± 0.0028 | 15.1 |
| D | 5 | 0.0055 ± 3.4e–4 | 61.5 |

To account for the photocatalytic effect enhancement by Ag-doping, the role of LSPR involved at the Ag clusters must be considered. Indeed, the association of silver with semiconducting photocatalysts has been already considered due to the strong LSPR effect under near visible light irradiation[29,30] and its efficient electron trapping ability.[31] The role of interfaces Ag-SC on the photocatalytic process can be understood based on the schematic representations of the electronic band structures related to Ag cluster embedded in host $BiVO_4$ SC[32] (Figure 9).

For $BiVO_4$ with the features of n-type semiconductor, its Fermi level $E_f$ is close to the conduction band energy level $E_{CB}$. Similarly, the Ag noble metal has a work function $\phi_m$ of 4.7 eV. Before their contact or embedded form, the fermi energy levels of semiconductor photocatalyst $E_{fsc}$ and that of the noble metal $E_{fM}$ are different as shown in Figure 9B. Once they come in-contact, schottky junction builds up while the electrons and holes rearrange in a new equilibrium state, where $E_{fsc}$ and $E_{fM}$ are aligned as shown in energy band diagram of Figure 9C. In this process, the electrons diffuse from the $BiVO_4$ to the Ag side and create a positively charged region with no free carriers in the $BiVO_4$ nanoparticle. This contributes to create a depletion region also known as space-charge region (SCR). In the equilibrium state, an equal amount of electrons are trapped in the adjacent Ag surface. This builds up an internal electrical field from the $BiVO_4$ side toward the Ag part preventing further movement of the carriers. When an electron–hole pair is photoexcited in or near the SCR region by an incident light, the internal electrical field E forces the electrons to move to the Ag region and the hole to the $BiVO_4$ region, preventing their recombination. The electrons and holes are then captured by the acceptors and donors in the solution, respectively, and initiate further redox reactions and improved photocatalytic efficiency.

Based on the above theoretical background analysis supported by Figure 9, Ag-SC composites based on Ag/$BiVO_4$ lead to photogenerated electron-hole pairs induced under visible light radiation and represent the key vectors for photocatalytic processes. The charge carrier density, their mobility and the lifetimes before their recombination process monitor the efficiency of photocatalytic reactions. For the charge carrier density, the intensity of electromagnetic field is enhanced by LSPR involved at the surface of metallic clusters. At Ag-SC interfaces, the schottky junctions are involved and enhance the density of photogenerated excitonic states. For the lifetime increase, apart from the LSPR effect, silver clusters are expected to trap the photogenerated electrons from $BiVO_4$ and leave the holes for the degradation reactions of organic species.

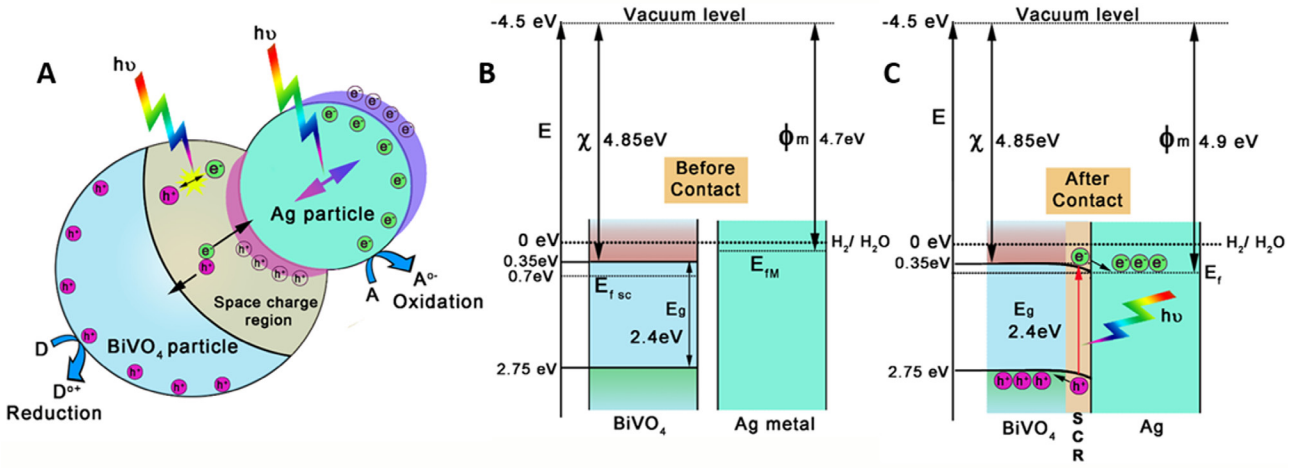


**Figure 9. A:** Schematic representation of photocatalysis mechanism of Ag/$BiVO_4$ M-SC nanocomposites. The presence of plasmonic effect induces a space charge region at the M-SC interfaces between $BiVO_4$ and Ag clusters. **B and C:** show the band bending with space charge region appear at the interfaces consecutive to alignment of Fermi levels.

## Conclusions

Ag/$BiVO_4$ nanocomposites were synthesized by high energy ball milling technique with different loading ratios of Ag (1, 3, 5 at.%). Structural properties were investigated by XRD, and Raman techniques demonstrating the occurrence of single phase with monoclinic scheelite symmetry. The composition and morphology of the synthesized powders were clarified by FE-SEM, EDX and HR-STEM techniques and evidences agglomerated particles of $BiVO_4$ with the involvement of Ag clusters. Electronic, dielectric and optical behaviors were studied and analyzed by complementary techniques. The electrical conductivity is marked by thermally activated values without net changes as a function of the incorporation of Ag in the composites. However, the interfacial polarization and the dynamic of charge transfer mechanism reflect the effect of Ag loading. Plasmonic Ag nanoclusters associated to $BiVO_4$ particles seem relevant to enhance the photocatalytic process based on the photo degradation of Acid blue 113 dyes in solution. The optimal concentration of Ag at 3at% was found through the high degradation rate constant by suppressing more than 90% of dyes within 45 mins under visible light radiation. Higher rates of Ag doping inhibit the photocatalytic degradation efficiencies probably due to inhomogeneous distribution of Ag clusters in the host media.

The supporting information associated with this article can be found online. It provides the details of experimental procedure for the synthesis of Ag doped and $BiVO_4$ based nanocomposites by ball milling route as well as the technical details of characterization techniques followed in our work.

## *Acknowledgements*

V. I. Merupo gratefully acknowledges the financial support given by CONACYT – Beca mixtas, Mexico and Doctoral School 3MPL – University of Maine, Le Mans, France. The authors would like to thank Prof. Alain Bulou for micro-Raman spectrometry measurements and Alvaro Angeles from LANE Cinvestav-IPN for HR-STEM characterization. We also acknowledge the financial support extended from the project between CINVESTAV and the University of Maine through their joint funds.

**Keywords:** Photocatalysis · Ag doping · $BiVO_4$ · plasmons · dielectric behavior

[1] Hashimoto K. , Irie H. , Fujishima A. , *Jpn. J. Appl. Phys.* **2005**, *44*, 8269–8285.
[2] Fujishima A. , Rao T. N. , Tryk D. A. , *J. Photochem. Photobiol. C Photochem. Rev.* **2000**, *1*, 1–21.
[3] Kudo A. , Ueda K. , Kato H. , Mikami I. , *Catal. Letters,* **1998**, *53*, 229–230.
[4] Zhao Z. , Li Z. , Zou Z. , *Phys. Chem. Chem. Phys.* **2011**, *13*, 4746–4753.
[5] Chen L. , Alarcón-Lladó E. , Hettick M. , Sharp I. D. , Lin, Y. , Javey A. , Ager J. W. , *J. Phys. Chem. C,* **2013**, *117*, 21635–21642.
[6] Li G. , Zhang D. , Yu J. C. , *Chem. Mater.* **2008**, *20*, 3983–3992.
[7] Frost R. L. , Henry D. A. , Weier M. L. , Martens, W. , *J. Raman Spectrosc.* **2006**, *37*, 722–732.
[8] Tokunaga S. , Kato H. , Kudo A. , *Chem. Mater.* **2001**, *13*, 4624–4628.
[9] Sandhya Kumari L. , Prabhakar Rao P. , Narayana Pillai Radhakrishnan A. , James V. , Sameera S. , Koshy P. , *Sol. Energy Mater. Sol. Cells* **2013**, *112*, 134–143.
[10] Ge L. , *J. Mol. Catal. A Chem.* **2008**, *282*, 62–66.
[11] Linic S. , Christopher P. , Ingram D. B. , *Nature Materials*, 2011, 10, 911–921.
[12] Zheng Z. , Huang B. , Qin X. , Zhang X. , Dai Y. , Whangbo M. H, *J.Mats Chem.*, 2011, 21, 9079.
[13] Thennarasu G. , Sivasamy A. , *Powder Technol.* **2013**, *250*, 1–12.
[14] Zhang A. , Zhang J. , *J. Alloys Compd.* **2010**, *491*, 631–635.
[15] Chen L. , Huang R. , Ma Y.J. , Luo S.L. , Au C.T. , Yin S. F. , *RSC Adv.* **2013**, *3*, 24354.
[16] Zhang X. H. , Ge L. , *Adv. Mats. Res*, 2009, 79–82, 2115–2118.
[17] Liu K. , Chang Z. , Li W. , Che P. , Zhou H. , *Sci. China Chem.* **2012**, *55*, 1770–1775.
[18] Zhang X. , Zhang Y. , Quan X. , Chen S. , *J. Hazard. Mater.* **2009**, *167*, 911–914.
[19] Merupo V.I. , Velumani S.; Ordon K. , Errien N. , Szade J. , Kassiba A.H. *CrystEngComm* **2015**, *17*, 3366–3375.
[20] Zhang A. , Zhang J. , *Appl. Surf. Sci.* **2010**, *256*, 3224–3227.

[21] Seery M. K. , George R. , Floris P. , Pillai S. C. , *J. Photochem. Photobiol. A Chem.* **2007**, *189*, 258–263.
[22] Thalluri S. M. , Martinez Suarez C. , Hussain M. , Hernandez S. , Virga A. , Saracco G. , Russo N. , *Ind. Eng. Chem. Res.* **2013**, *52*, 17414–17418.
[23] Yu J. , Kudo A. , *Adv. Funct. Mater.* **2006**, *16*, 2163–2169.
[24] Rycenga M. , Cobley C. M. , Zeng J. , Li W. , Moran C. H. , Zhang Q. , Qin D. , Xia Y. , *Chemical Reviews,* **2011**, *111*, 3669–3712.
[25] Zhang H. , Wang G. , Chen D. , Lv X. , Li J. , *Chemical Materials.* **2008**, 6543–6549.
[26] Havriliak S. , Negami S. , *J. Polym. Sci. Part C Polym. Symp.* **2007**, *14*, 99–117.
[27] Venkatesan R. , Velumani S. , Tabellout M. , Errien N. , Kassiba A. , *Journal of Physics and Chemistry of Solids*, **2013**, 74, 12,1695–1702.
[28] IARC (World Health Organization International Agency for Research on Cancer), *Some Ind. Chem. Dyest.* **1982**, 29.
[29] Kuriakose S.; Choudhary, V.; Satpati, B.; Mohapatra, S. *Beilstein J. Nanotechnol.* **2014**, *5*, 639–650.
[30] Chen X. , Zheng Z. , Ke X. , Jaatinen E. , Xie T. , Wang D. , Guo C. , Zhao J. , Zhu H. , *Green Chemistry*, 2010, 12, 414.
[31] Xin B. , Jing L. , Ren Z. , Wang B. , Fu H. , *J. Phys. Chem. B* **2005**, *109*, 2805–2809.
[32] Zhang X, Chen Y L, Liu Ru-Shi and Tsai D P. , *Rep. Prog. Phys.* **2013**, 76, 046401 (41pp).

Submitted: February 4, 2016
Accepted: April 18, 2016